SINTEF
PROCEEDINGS
2

Proceedings of the 12th International Conference on Computational Fluid Dynamics in the Oil & Gas, Metallurgical and Process Industries

Progress in Applied CFD – CFD2017

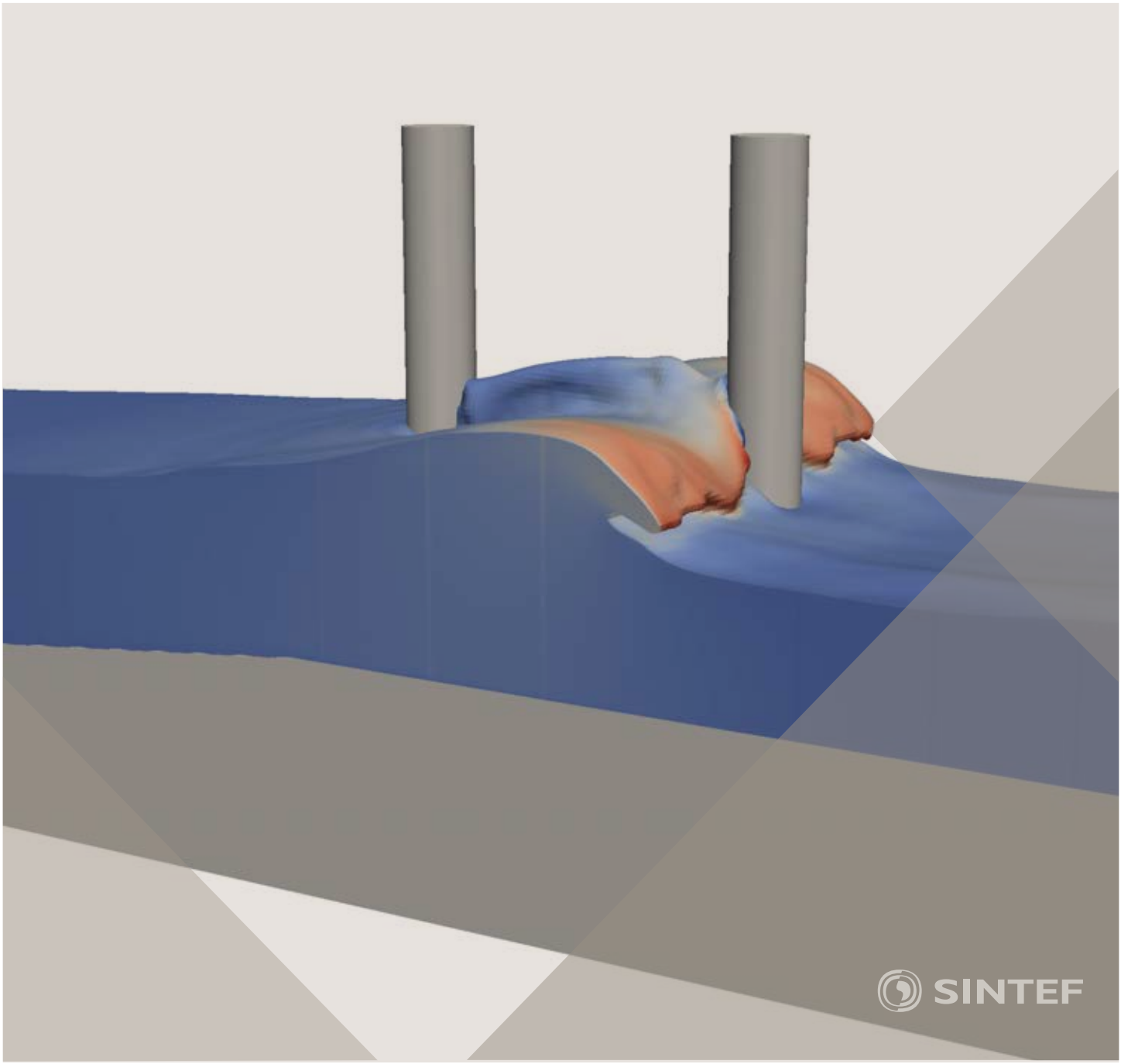

SINTEF Proceedings

Editors:
Jan Erik Olsen and Stein Tore Johansen

Progress in Applied CFD – CFD2017

Proceedings of the 12th International Conference on Computational Fluid Dynamics in the Oil & Gas, Metallurgical and Process Industries

SINTEF Academic Press

SINTEF Proceedings no 2
Editors: Jan Erik Olsen and Stein Tore Johansen
Progress in Applied CFD – CFD2017
Selected papers from 10th International Conference on Computational Fluid Dynamics in the Oil & Gas, Metallurgical and Process Industries

Key words:
CFD, Flow, Modelling

Cover, illustration: Arun Kamath

ISSN 2387-4295 (online)
ISBN 978-82-536-1544-8 (pdf)

SINTEF Academic Press
Address: Forskningsveien 3 B
PO Box 124 Blindern
N-0314 OSLO
Tel: +47 73 59 30 00
Fax: +47 22 96 55 08

www.sintef.no/byggforsk
www.sintefbok.no

SINTEF Proceedings
SINTEF Proceedings is a serial publication for peer-reviewed conference proceedings on a variety of scientific topics.
The processes of peer-reviewing of papers published in SINTEF Proceedings are administered by the conference organizers and proceedings editors. Detailed procedures will vary according to custom and practice in each scientific community.

PREFACE

This book contains all manuscripts approved by the reviewers and the organizing committee of the 12th International Conference on Computational Fluid Dynamics in the Oil & Gas, Metallurgical and Process Industries. The conference was hosted by SINTEF in Trondheim in May/June 2017 and is also known as CFD2017 for short. The conference series was initiated by CSIRO and Phil Schwarz in 1997. So far the conference has been alternating between CSIRO in Melbourne and SINTEF in Trondheim. The conferences focuses on the application of CFD in the oil and gas industries, metal production, mineral processing, power generation, chemicals and other process industries. In addition pragmatic modelling concepts and bio-mechanical applications have become an important part of the conference. The papers in this book demonstrate the current progress in applied CFD.

The conference papers undergo a review process involving two experts. Only papers accepted by the reviewers are included in the proceedings. 108 contributions were presented at the conference together with six keynote presentations. A majority of these contributions are presented by their manuscript in this collection (a few were granted to present without an accompanying manuscript).

The organizing committee would like to thank everyone who has helped with review of manuscripts, all those who helped to promote the conference and all authors who have submitted scientific contributions. We are also grateful for the support from the conference sponsors: ANSYS, SFI Metal Production and NanoSim.

Stein Tore Johansen & Jan Erik Olsen

Organizing committee:

Conference chairman: Prof. Stein Tore Johansen
Conference coordinator: Dr. Jan Erik Olsen
Dr. Bernhard Müller
Dr.Sigrid Karstad Dahl
Dr.Shahriar Amini
Dr.Ernst Meese
Dr.Josip Zoric
Dr.Jannike Solsvik
Dr.Peter Witt

Scientific committee:

Stein Tore Johansen, SINTEF/NTNU
Bernhard Müller, NTNU
Phil Schwarz, CSIRO
Akio Tomiyama, Kobe University
Hans Kuipers, Eindhoven University of Technology
Jinghai Li, Chinese Academy of Science
Markus Braun, Ansys
Simon Lo, CD-adapco
Patrick Segers, Universiteit Gent
Jiyuan Tu, RMIT
Jos Derksen, University of Aberdeen
Dmitry Eskin, Schlumberger-Doll Research
Pär Jönsson, KTH
Stefan Pirker, Johannes Kepler University
Josip Zoric, SINTEF

CONTENTS

PRAGMATIC MODELLING 9
On pragmatism in industrial modeling. Part III: Application to operational drilling 11
CFD modeling of dynamic emulsion stability 23
Modelling of interaction between turbines and terrain wakes using pragmatic approach 29

FLUIDIZED BED 37
Simulation of chemical looping combustion process in a double looping fluidized bed reactor with cu-based oxygen carriers 39
Extremely fast simulations of heat transfer in fluidized beds 47
Mass transfer phenomena in fluidized beds with horizontally immersed membranes 53
A Two-Fluid model study of hydrogen production via water gas shift in fluidized bed membrane reactors 63
Effect of lift force on dense gas-fluidized beds of non-spherical particles 71
Experimental and numerical investigation of a bubbling dense gas-solid fluidized bed 81
Direct numerical simulation of the effective drag in gas-liquid-solid systems 89
A Lagrangian-Eulerian hybrid model for the simulation of direct reduction of iron ore in fluidized beds 97
High temperature fluidization - influence of inter-particle forces on fluidization behavior 107
Verification of filtered two fluid models for reactive gas-solid flows 115

BIOMECHANICS 123
A computational framework involving CFD and data mining tools for analyzing disease in cartoid artery 125
Investigating the numerical parameter space for a stenosed patient-specific internal carotid artery model 133
Velocity profiles in a 2D model of the left ventricular outflow tract, pathological case study using PIV and CFD modeling 139
Oscillatory flow and mass transport in a coronary artery 147
Patient specific numerical simulation of flow in the human upper airways for assessing the effect of nasal surgery 153
CFD simulations of turbulent flow in the human upper airways 163

OIL & GAS APPLICATIONS 169
Estimation of flow rates and parameters in two-phase stratified and slug flow by an ensemble Kalman filter 171
Direct numerical simulation of proppant transport in a narrow channel for hydraulic fracturing application 179
Multiphase direct numerical simulations (DNS) of oil-water flows through homogeneous porous rocks 185
CFD erosion modelling of blind tees 191
Shape factors inclusion in a one-dimensional, transient two-fluid model for stratified and slug flow simulations in pipes 201
Gas-liquid two-phase flow behavior in terrain-inclined pipelines for wet natural gas transportation 207

NUMERICS, METHODS & CODE DEVELOPMENT 213
Innovative computing for industrially-relevant multiphase flows 215
Development of GPU parallel multiphase flow solver for turbulent slurry flows in cyclone 223
Immersed boundary method for the compressible Navier–Stokes equations using high order summation-by-parts difference operators 233
Direct numerical simulation of coupled heat and mass transfer in fluid-solid systems 243
A simulation concept for generic simulation of multi-material flow, using staggered Cartesian grids 253
A cartesian cut-cell method, based on formal volume averaging of mass, momentum equations 265
SOFT: a framework for semantic interoperability of scientific software 273

POPULATION BALANCE 279
Combined multifluid-population balance method for polydisperse multiphase flows 281
A multifluid-PBE model for a slurry bubble column with bubble size dependent velocity, weight fractions and temperature 285
CFD simulation of the droplet size distribution of liquid-liquid emulsions in stirred tank reactors 295
Towards a CFD model for boiling flows: validation of QMOM predictions with TOPFLOW experiments 301
Numerical simulations of turbulent liquid-liquid dispersions with quadrature-based moment methods 309
Simulation of dispersion of immiscible fluids in a turbulent couette flow 317
Simulation of gas-liquid flows in separators - a Lagrangian approach 325
CFD modelling to predict mass transfer in pulsed sieve plate extraction columns 335

BREAKUP & COALESCENCE 343
Experimental and numerical study on single droplet breakage in turbulent flow 345
Improved collision modelling for liquid metal droplets in a copper slag cleaning process 355
Modelling of bubble dynamics in slag during its hot stage engineering 365
Controlled coalescence with local front reconstruction method 373

BUBBLY FLOWS 381
Modelling of fluid dynamics, mass transfer and chemical reaction in bubbly flows 383
Stochastic DSMC model for large scale dense bubbly flows 391
On the surfacing mechanism of bubble plumes from subsea gas release 399
Bubble generated turbulence in two fluid simulation of bubbly flow 405

HEAT TRANSFER 413
CFD-simulation of boiling in a heated pipe including flow pattern transitions using a multi-field concept 415
The pear-shaped fate of an ice melting front 423
Flow dynamics studies for flexible operation of continuous casters (flow flex cc) 431
An Euler-Euler model for gas-liquid flows in a coil wound heat exchanger 441

NON-NEWTONIAN FLOWS 449
Viscoelastic flow simulations in disordered porous media 451
Tire rubber extrudate swell simulation and verification with experiments 459
Front-tracking simulations of bubbles rising in non-Newtonian fluids 469
A 2D sediment bed morphodynamics model for turbulent, non-Newtonian, particle-loaded flows 479

METALLURGICAL APPLICATIONS 491
Experimental modelling of metallurgical processes 493
State of the art: macroscopic modelling approaches for the description of multiphysics phenomena within the electroslag remelting process 499
LES-VOF simulation of turbulent interfacial flow in the continuous casting mold 507
CFD-DEM modelling of blast furnace tapping 515
Multiphase flow modelling of furnace tapholes 521
Numerical predictions of the shape and size of the raceway zone in a blast furnace 531
Modelling and measurements in the aluminium industry - Where are the obstacles? 541
Modelling of chemical reactions in metallurgical processes 549
Using CFD analysis to optimise top submerged lance furnace geometries 555
Numerical analysis of the temperature distribution in a martensic stainless steel strip during hardening 565
Validation of a rapid slag viscosity measurement by CFD 575
Solidification modeling with user defined function in ANSYS Fluent 583
Cleaning of polycyclic aromatic hydrocarbons (PAH) obtained from ferroalloys plant 587
Granular flow described by fictitious fluids: a suitable methodology for process simulations 593
A multiscale numerical approach of the dripping slag in the coke bed zone of a pilot scale Si-Mn furnace 599

INDUSTRIAL APPLICATIONS 605
Use of CFD as a design tool for a phospheric acid plant cooling pond 607
Numerical evaluation of co-firing solid recovered fuel with petroleum coke in a cement rotary kiln: Influence of fuel moisture 613
Experimental and CFD investigation of fractal distributor on a novel plate and frame ion-exchanger 621

COMBUSTION 631
CFD modeling of a commercial-size circle-draft biomass gasifier 633
Numerical study of coal particle gasification up to Reynolds numbers of 1000 641
Modelling combustion of pulverized coal and alternative carbon materials in the blast furnace raceway 647
Combustion chamber scaling for energy recovery from furnace process gas: waste to value 657

PACKED BED 665
Comparison of particle-resolved direct numerical simulation and 1D modelling of catalytic reactions in a packed bed 667
Numerical investigation of particle types influence on packed bed adsorber behaviour 675
CFD based study of dense medium drum separation processes 683
A multi-domain 1D particle-reactor model for packed bed reactor applications 689

SPECIES TRANSPORT & INTERFACES 699
Modelling and numerical simulation of surface active species transport - reaction in welding processes 701
Multiscale approach to fully resolved boundary layers using adaptive grids 709
Implementation, demonstration and validation of a user-defined wall function for direct precipitation fouling in Ansys Fluent 717

FREE SURFACE FLOW & WAVES 727
Unresolved CFD-DEM in environmental engineering: submarine slope stability and other applications 729
Influence of the upstream cylinder and wave breaking point on the breaking wave forces on the downstream cylinder 735
Recent developments for the computation of the necessary submergence of pump intakes with free surfaces 743
Parallel multiphase flow software for solving the Navier-Stokes equations 752

PARTICLE METHODS 759
A numerical approach to model aggregate restructuring in shear flow using DEM in Lattice-Boltzmann simulations 761
Adaptive coarse-graining for large-scale DEM simulations 773
Novel efficient hybrid-DEM collision integration scheme 779
Implementing the kinetic theory of granular flows into the Lagrangian dense discrete phase model 785
Importance of the different fluid forces on particle dispersion in fluid phase resonance mixers 791
Large scale modelling of bubble formation and growth in a supersaturated liquid 798

FUNDAMENTAL FLUID DYNAMICS 807
Flow past a yawed cylinder of finite length using a fictitious domain method 809
A numerical evaluation of the effect of the electro-magnetic force on bubble flow in aluminium smelting process 819
A DNS study of droplet spreading and penetration on a porous medium 825
From linear to nonlinear: Transient growth in confined magnetohydrodynamic flows 831

SHAPE FACTORS INCLUSION IN A ONE-DIMENSIONAL, TRANSIENT TWO-FLUID MODEL FOR STRATIFIED AND SLUG FLOW SIMULATIONS IN PIPES

Arianna BONZANINI[1]*, **Davide PICCHI**[2]†, **Marco FERRARI**[3]‡, **Pietro POESIO**[1]§

[1]Università degli Studi di Brescia, Dipartimento di Ingegneria Meccanica ed Industriale, Via Branze, 38, 25123 Brescia, ITALY

[2]Tel-Aviv University, Faculty of Engineering, School of Mechanical Engineering Ramat Aviv, 69978 Tel-Aviv, ISRAEL

[3]Politecnico di Milano, PoliMi Department of Mathematics, 20133 Milan, ITALY

* E-mail: a.bonzanini001@unibs.it
† E-mail: davide.picchi@gmail.com
‡ E-mail: marco2.ferrari@polimi.it
§ E-mail: pietro.poesio@unibs.it

ABSTRACT

In previous works, (Ferrari *et al.*, 2017) have shown that a one-dimensional, hyperbolic, transient five equations two-fluid model is able to numerically describe stratified, wavy, and slug flow in horizontal and near-horizontal pipes. Slug statistical characteristics, such as slug velocity, frequency, and length can be numerically predicted with results in good agreement with experimental data and well-known empirical relations. In this model some approximated and simplified assumptions are adopted to describe shear stresses at wall and at phase interface.

In this paper, we focus on the possibility to account for the cross sectional flow by including the shape of the velocity profiles, inserting shape factors into the momentum balance equations. Velocity profiles are obtained by the pre-integrated model proposed by (Biberg, 2007) and they are computed at each time step and at each computational cell. Once that the velocity profiles are known, the obtained shape factors are inserted in the numerical resolution. In this way it is possible to recover part of the information lost due to the one-dimensional flow description.

Velocity profiles computed in stratified conditions are compared against experimental profiles measured with PIV technique - see (Ayati *et al.*, 2015), showing good agreement. Finally, first results in slug flow configuration are shown.

Keywords: Multiphase pipeline transport, Oil & Gas .

NOMENCLATURE

Greek Symbols

α	Phase volume fraction, $[-]$
β	Wetted angle, $[rad]$
γ	Shape factor, $[-]$
δ	Boundary layer thickness, $[m]$
θ	Pipe inclination angle, $[rad]$
$\boldsymbol{\lambda}$	Eigenvalues vector, $[m/s]$
μ	Dynamic viscosity, $[kg/ms]$
ρ	Mass density, $[kg/m^3]$
τ	Shear stress, $[Pa]$

Latin Symbols

A	Pipe section, $[m^2]$.
A_j	Pipe section occupied by phase j, $[m^2]$.
c	Sound speed, $[m/s]$.
D	Pipe diameter, $[m]$.
f	Friction factor, $[-]$.
F_i	Interfacial friction term, $[N/m^3]$.
F_w	Wall friction term, $[N/m^3]$.
g	Gravity acceleration, $[m/s^2]$.
h	Liquid height, $[m]$.
k_s	Sand roughness, $[m]$.
p_i	Interfacial pressure, $[Pa]$.
r_p	Pressure relaxation parameter, $[1/Pas]$.
$\mathbf{R}$	Eigenvector matrix, $[m/s]$.
Re	Reynolds number, $[-]$.
S_j	Pipe perimeter wetted by phase j, $[m]$.
S_i	Interfacial perimeter, $[m]$.
t	Time coordinate, $[s]$.
u	Phase velocity, $[m/s]$.
u_i	Interfacial velocity, $[m/s]$.
u_s	Superficial velocity, $[m/s]$.
v	Cross-sectional velocity, $[m/s]$.
x	Space coordinate in the axial direction, $[m]$.
y	Space coordinate in the cross-sectional direction, $[m]$.

Sub/superscripts

g	Gas phase.
l	Liquid phase.
j	Generic phase, gas or liquid.

INTRODUCTION

Stratified and slug flow are two-phase flow regimes frequently encountered in multiphase pipeline transport of oil and gas. In the past decades, the interest in the numerical description of these flow regimes has significantly increased, aiming at obtaining predictions about the behaviour of the fluids employed in petroleum transport pipelines, chemical and nuclear industries, and buoyancy driven fermentation devices. The one-dimensional averaged two-fluid model is often employed (see (Issa and Kempf, 2003), (Renault, 2007)) and pipelines are usually simulated adopting mono-dimensional models to keep reasonable simulation times. Closure relations to describe shear stresses at interface and at wall are required, and friction factors are often described adopting models or correlations (see (Bonizzi *et al.*, 2009)); however, wall and interfacial shear stresses are related via the velocity distribution and, therefore, the cross-sectional flow description is required to obtain consistent modelling. Two-dimensional and three-dimensional models are computationally expensive and require too long computational times; to solve the issue of speed versus consistency, the cross-sectional velocity profiles can be described by a pre-integrated model, which leads to a consistent set of near-

algebraic friction models suitable for one-dimensional two-phase flow simulations.

In the present work, we aim at introducing the velocity profiles shape description in the mono-dimensional, transient, five-equation two-fluid model by (Ferrari *et al.*, 2017): they assumed that the profiles coefficients were unitary ($\gamma_l = \gamma_g = 1$), representing a completely flat profile. The profiles coefficients are correction factors adopted to describe the curvature of the velocity profile, since the latter is not constant over the entire cross section and, for turbulent flows, the profile coefficient is slightly above one. To account for the cross-sectional velocity, we need to modify the five-equation system eigenstructure, inserting the γ factors in the modelisation; then, we adopted the pre-integrated model developed by (Biberg, 2007), to describe the shear stresses at interface and at wall consistently with the modelling of the velocity profiles.

In this paper, the comparison of the computed velocity profiles against the experimental ones measured by (Ayati *et al.*, 2015) will be reported, showing a fairly good agreement; then, first results in slug flow will be presented, showing how to describe numerically the velocity profiles during the transition from two-phase to single phase flow.

MODEL DESCRIPTION

In this work, we adopted the mono-dimensional, hyperbolic, transient, five-equation, two-fluid model proposed by (Ferrari *et al.*, 2017), which is able to compute well flow regimes transitions and slug flow characteristics. The first modification performed on the model consists in adding the shape factors γ_g and γ_l, both for gas and liquid phase, in the momentum balance equations, Eqs. (4) - (5)

$$\frac{\partial \alpha_g}{\partial t} + u_i \frac{\partial \alpha_g}{\partial x} = r_p(p_{ig} - p_{il}) \tag{1}$$

$$\frac{\partial(\alpha_g \rho_g)}{\partial t} + \frac{\partial(\alpha_g \rho_g u_g)}{\partial x} = 0 \tag{2}$$

$$\frac{\partial(\alpha_l \rho_l)}{\partial t} + \frac{\partial(\alpha_l \rho_l u_l)}{\partial x} = 0 \tag{3}$$

$$\frac{\partial(\alpha_g \rho_g u_g)}{\partial t} + \frac{\partial(\gamma_g \alpha_g \rho_g u_g^2)}{\partial x} + \alpha_g \frac{\partial p_{ig}}{\partial x} + \rho_g \alpha_g g \frac{\partial h}{\partial x} \cos(\theta) = -\rho_g \alpha_g g \sin(\theta) - F_{wg} - F_i \tag{4}$$

$$\frac{\partial(\alpha_l \rho_l u_l)}{\partial t} + \frac{\partial(\gamma_l \alpha_l \rho_l u_l^2)}{\partial x} + \alpha_l \frac{\partial p_{il}}{\partial x} + \rho_l \alpha_l g \frac{\partial h}{\partial x} \cos(\theta) = -\rho_l \alpha_l g \sin(\theta) - F_{wl} + F_i. \tag{5}$$

The introduction of the shape factors in the model equations modifies the eigenstructure of the system; since the numerical resolution of the model is based on the Roe linearisation, the knowledge of the system eigenstructure is required. Thus, as first step of this work, the modified eigenvalue and eigenvectors were computed; we remark that, if the shape factors in the modified eigenstructure are set to one (as supposed in the previous work by (Ferrari *et al.*, 2017)), the original version of the eigenstructure is recovered (the comparison of the old eigenvalues against the new ones including shape factors is reported in Appendix A). The numerical resolution is largely based on the one proposed by (Ferrari *et al.*, 2017), which adopts the finite volume method and an explicit first order time discretisation. The source term on the right-hand side of the advection equation –Eq. (1) – is taken into account by a pressure relaxation process, described by (Munkejord, 2005), which requires the solution of a second degree polynomial equation: in the hyperbolic step, the gas volume fraction α_g is modified to restore pressure equality at the interface. Some modifications were applied in the computation of the shear stresses at wall and at interface and the pre-integrated model proposed by (Biberg, 2007) was adopted to compute the cross-sectional velocity profiles, which are required to obtain the shape factors (see (Picchi *et al.*, 2014))

$$\gamma_j = \frac{1}{A_j v_j^2} \int v_j^2(y) dA. \tag{6}$$

The velocity distribution v_j in the y direction is computed as proposed by (Biberg, 2007)

$$v_j = sgn(\tau_{wj}) \frac{u^*}{\kappa} \Delta_j + C_j, \tag{7}$$

where Δ_j and C_j, reported in Appendix B, are function of Y, the adimensional position along the pipe cross section, of R_j, the ratio between the shear stress at interface and at wall,

$$Y = \frac{y}{h}, \qquad R_j = \frac{\tau_i}{\tau_{wj}} \tag{8}$$

and of K_j, a parameter accounting for the interface shape, which reads, respectively for gas and liquid phase,

$$K_g = \frac{8\nu_g}{|u_g - u_l|}, \quad K_l = 1 \tag{9}$$

in case of smooth interface, and

$$K_g = \frac{0.065\rho_g}{\rho_l - \rho_g} \frac{u_g - u_l}{g\bar{h}_g cos\theta}, \quad K_l = 10\sqrt{\frac{\rho_g}{\rho_l}} \left| \frac{u_g - u_l}{u_l} \right| \tag{10}$$

in case of wavy interface.

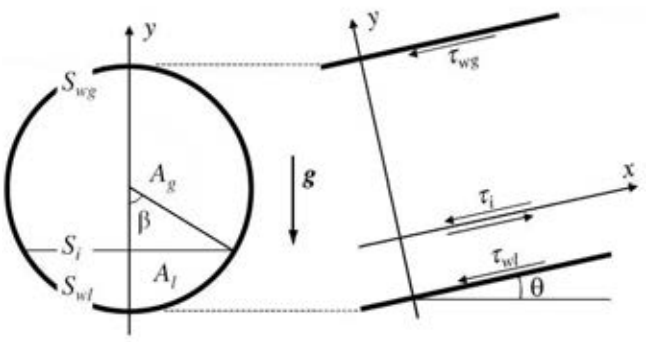

Figure 1: Schematic diagram of geometry.

The parameters R_j and K_j are introduced also in the computation of the shear stresses at wall and at interface through the corrected hydraulic diameter proposed by (Biberg, 2007)

$$D_{ej} = \frac{4A_j}{S_{wj}} \left(\frac{S_{wj}}{S_{wj} + S_i} \right)^{F(R_j, K_j)}, \tag{11}$$

where the wetted perimeter S_{wl} and S_{wg} and the interface perimeter S_i are shown in Figure 1. The corrected hydraulic diameter is employed to compute the Reynolds number

$$Re_j = |u_j| \frac{\rho_j}{\mu_j} D_{ej}, \tag{12}$$

which is then used to obtain the friction factor f_j by the Colebrook-White interpolation

$$\frac{1}{\sqrt{f_j}} = -2\log_{10}\left(\frac{2.51}{Re_j \sqrt{f_j}} + \frac{k_s}{3.7D} \right) \tag{13}$$

in the case of turbulent flow and

$$f_j = \frac{64}{Re_j} \tag{14}$$

in the case of laminar flow. In this work, both smooth and rough flow can be described thanks to the sand roughness k_s. The gas shear stress at wall is computed as

$$\tau_{wg} = \frac{f_g}{4}\frac{\rho_g |u_g| u_g}{2}; \tag{15}$$

the value of τ_i and τ_{wl} are computed by knowing τ_{wg}, R_g and R_l.
The value of R_g is computed in every computational cell and at every time step by a root search algorithm, imposing the equality of gas and liquid velocity at the interface, while computing the shear stresses. Once that R_g is known, it is possible to obtain the velocity profile in the cross-sectional direction and, by integration, the shape factors value, which will be inserted in the Roe matrix in the subsequent time step.

RESULTS

Stratified flow

In this Section, the computed cross-sectional velocity profiles in stratified flow conditions will be validated against the experimental measurements performed by (Ayati *et al.*, 2015): the geometry adopted in the experiments consists in a horizontal 31 m long PVC pipe, with an internal diameter $D = 0.1$ m; the fluids used in the test cases are water and air at 22 $^\circ C$, whose density are, respectively, 997 kg/m^3 and 1.2 kg/m^3.
Concerning the numerical simulations, the space discretisation consists in 620 cells, leading to a $\Delta x = D/2$; the time step is $\Delta t = 10^{-5}$ s, with a corresponding CFL

$$CFL = \frac{\Delta t}{\Delta x}|\lambda_{max}| \approx 0.2, \tag{16}$$

since the maximum eigenvalue is approximately 10^3 m/s (for further information on the eigenvalues, see Appendix A).
We perform four comparisons, with four different couples of superficial velocities, which are reported in Table 1: two of the chosen configurations are characterized by a smooth sub-regime and two by a 2D waves sub-regime, as stated by (Ayati *et al.*, 2015). In the case of smooth sub-regime (and therefore smooth interface), in our numerical simulations we adopted the relation for K_f in Equation (9), while in case of 2D waves, we employed Equation (10). The PVC pipe roughness, required in Equation (13), was set to the representative value $5 \cdot 10^{-3} mm$, since the actual value is not reported by (Ayati *et al.*, 2015).
(Ayati *et al.*, 2015) perform the PIV measurements in a vertical plane located at $260D$ downstream from inlet and, thus, our numerical results are extracted at the same position along the pipe.
Figures 2 and 3 compare the experimental results with the numerical ones: we can observe that the shapes of the computed velocity profiles are in good agreement with the experimental one (the experimental profiles present some discontinuities because of strong background reflections or restricted optical access in proximity of the interface, as explained by (Ayati *et al.*, 2015)). In the case of smooth regime, there is a small discrepancy in the velocity magnitude: this can be due to the fact that the numerical code forecasts an equilibrium liquid volume fraction slightly higher than the one observed in the experiments: therefore, the flow section for the gas phase is smaller and the velocity at the nose of the profile is higher, while the opposite happens for the liquid phase, whose velocity magnitude of the flat profile is slightly lower than the observed one.

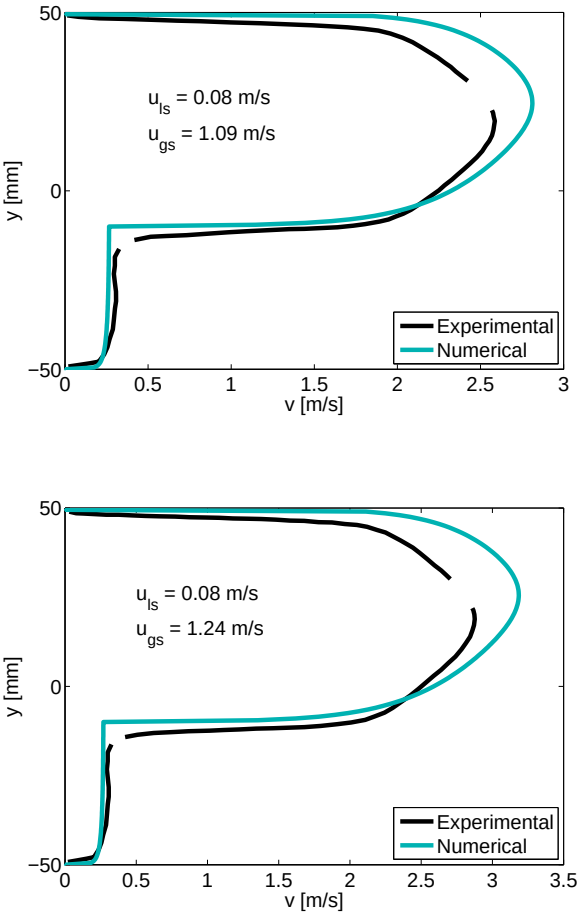

Figure 2: Comparison of the experimental and the numerical profiles. Smooth sub-regime.

In Table 1 the computed shape factor for gas and liquid phase are reported.

Table 1: Superficial liquid and gas velocities adopted in the numerical simulations.

u_{ls} $[m/s]$	u_{gs} $[m/s]$	Sub-regime	γ_l	γ_g
0.08	1.09	Smooth	1.10	1.03
0.08	1.27	Smooth	1.09	1.04
0.10	2.03	2D waves	1.09	1.04
0.10	2.29	2D waves	1.10	1.04

Slug flow

First results in slug flow configuration will be now discussed. For the numerical simulations in slug conditions, the adopted geometry consists in a 36 m long pipe, with and internal diameter $D = 0.078$ m (see (Issa and Kempf, 2003)); in this case we adopt $\Delta x = 0.577D$ and $\Delta t = 10^{-5}$ s. The liquid and gas superficial velocities are, respectively, $u_ls = 1.5m/s$ and $u_gs = 2.0m/s$; the simulated fluids are again water and air.

(Ferrari *et al.*, 2017) developed a criterion to simulate the transition from two-phase to single phase flow, which takes place as a slug emerges and grows: this method consists in setting to zero the gas velocity when the gas volume fraction drops under a certain threshold; the threshold value is in the range $3 \div 8 \cdot 10^{-3}$. A special treatment for the shape factors and velocity profile inside the slug body was added to the existing transition criterion: this method prescribes that, when a slug forms, the shape factor of the gas phase is no longer computed, since it is no more required in the calculation concerning the gas momentum balance equation. Regarding the liquid phase, we prescribe that the velocity profile inside the slug body follow the relation proposed by (Biberg, 2007) in the case of Poiseuille-type flow: although this kind of flow is normally laminar, thanks to the turbulent viscosity employed in the computations, we obtain a turbulent shaped profile.
(Dukler *et al.*, 1985) adopted the one-seventh power law to describe the velocity profile in the slug body

$$v_l = v_0 \left(\frac{y}{\delta} \right)^{1/7}. \tag{17}$$

and, later, (Gopal and Jepson, 1997) supported their assumptions by experimental observations. In Figure 4 the computed profile in a slug body is compared against the one-seventh power law profile, which was calculated with $\delta = D/2$ and $v_0 = u_{ls} + u_{gs} = 3.5\ m/s$: this choice is justified by the fact that the centerline velocity v_0 is very close to the slug velocity, which is obtained by summing the gas and liquid superficial velocities, as reported by (Jepson, 1989). The shape factor in the slug body is in the range $1.02 \div 1.04$.

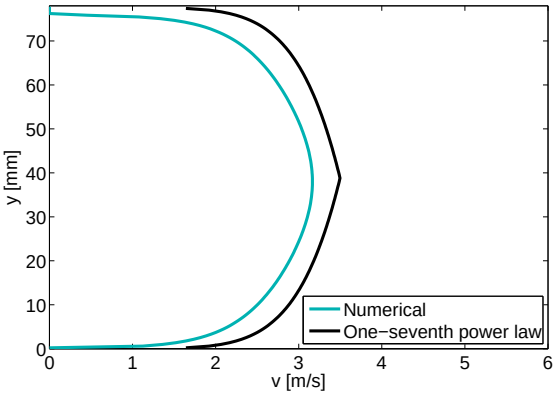

Figure 4: Comparison of the one-seventh power law profile against the computed one.

Finally, Figure 5 reports the qualitative behaviour of the velocity profiles before (top) and after (bottom) slug formation.

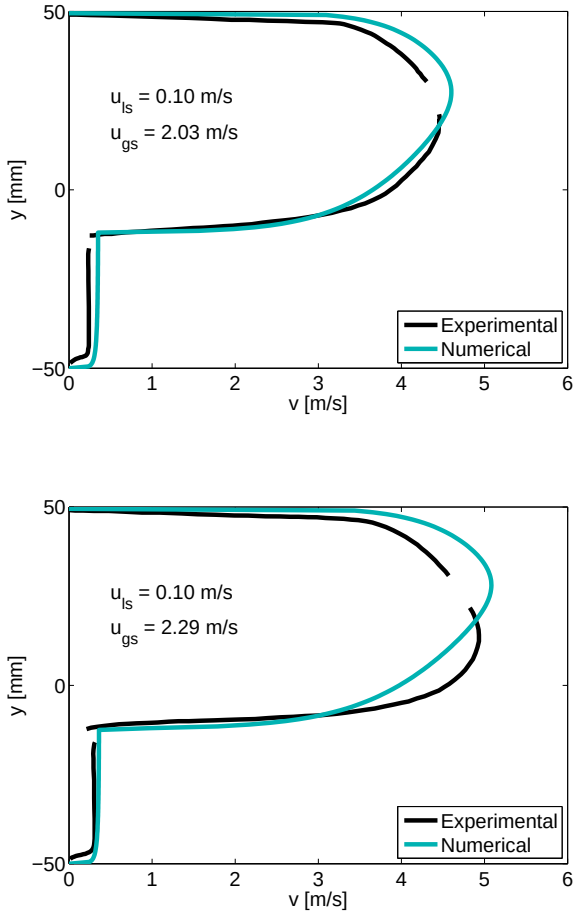

Figure 3: Comparison of the experimental and the numerical profiles. 2D waves sub-regime.

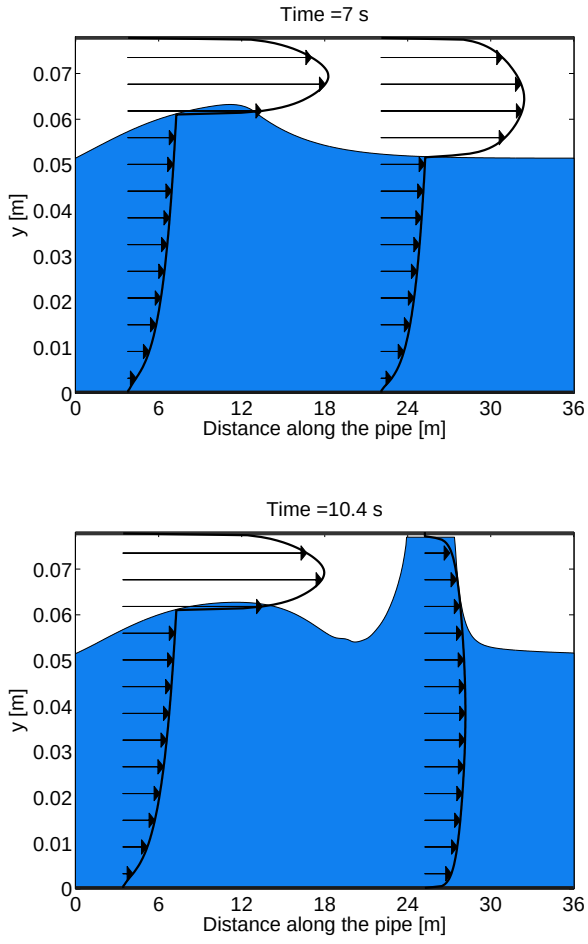

Figure 5: Example of computed velocity profiles before (top) and after (bottom) slug formation.

CONCLUSION

In this work, a transient, five-equation two-fluid model accounting for cross-sectional velocity distribution has been presented. Starting from the existing numerical code by (Ferrari *et al.*, 2017), the model has been modified to account for the velocity profiles shape by the γ factor in the momentum balance equations; the inclusion of these correction coefficients modifies the five-equation system eigenstructure, which explicit form has been computed including γ factors. The pre-integrated model proposed by (Biberg, 2007) has been embodied in the numerical code, to compute shear stresses at wall and at interface and to obtain a consistent description of the cross-sectional velocity distribution.
Numerical results both in stratified and in slug flow regime have been presented. The computed velocity profiles in smooth and wavy stratified regime were compared against experimental measurements, showing good agreement. Moreover, a method to compute the velocity profile during the transition from two-phase to single phase flow (which occurs during slug formation) has been developed; the computed velocity distribution in the liquid phase follows quite accurately the one-seventh power law profile, which has been experimentally observed to occur in the slug body.

REFERENCES

AYATI, A., KOLAAS, J. and JOHNSON, G. (2015). "Combined simultaneous two-phase piv and interface elevation measurements in stratified gas/liquid pipe flow". *International Journal of Multiphase Flow*, **74**, 45 – 58.

BIBERG, D. (2007). "A mathematical model for two-phase stratified turbulent duct flow". *Multiphase Science and Technology*, **19**, 1 – 48.

BONIZZI, M., ANDREUSSI, P. and BANERJEE, S. (2009). "Flow regime independent, high resolution multi-field modelling of near-horizontal gas-liquid flows in pipelines". *International Journal of Multiphase Flow*, **35**, 34 – 46.

DUKLER, A.E., MOALEM MARON, D. and BRAUNER, N. (1985). "A physical model for predicting the minumum stable slug length". *Chemical Engineering Science*, **40**, 1379 – 1385.

FERRARI, M., BONZANINI, A. and POESIO, P. (2017). "A five-equation, transient, hyperbolic, one-dimensional model for slug capturing in pipes". *International Journal for Numerical Method in Fluids*. Accepted for publication.

GOPAL, M. and JEPSON, W.P. (1997). "Development of digital image analysis techniques for the study of velocity and void profiles in slug flow." *International Journal of Multiphase Flow*, **23**, 945 – 965.

ISSA, R.I. and KEMPF, M.H.W. (2003). "Simulation of slug flow in horizontal and nearly horizontal pipes with the two-fluid model". *International Journal of Multiphase Flow*, **29**, 69 – 95.

JEPSON, W.P. (1989). "Modelling the transition to slug flow in horizontal conduit". *Canadian Journal of Chemical Engineering*, **67**, 731 – 740.

MUNKEJORD, S.T. (2005). *Analysis of the two-fluid model and the drift-flux model for numerical calculation of two-phase flow*, vol. Phd Thesis 2005, NTNU, Trondheim, Norway.

PICCHI, D., CORRERA, S. and POESIO, P. (2014). "Flow pattern transition, pressure gradient, hold-up predictions in gas/non-newtonian power-law fluid stratified flow". *International Journal of Multiphase Flow*, **63**, 105 – 115.

RENAULT, F. (2007). *A lagrangian slug capturing scheme for gas-liquid flows in pipes*, vol. Phd Thesis 2005, NTNU, Trondheim, Norway.

APPENDIX A: COMPARISON OF THE EIGENSTRUCTURE WITH AND WITHOUT THE INCLUSION OF THE SHAPE FACTORS IN THE MODEL

We report here the eigenvalues and the eigenvectors of the five-equation system with and without the shape factor inclusion in the model, to show how deeply the description of the velocity profiles affects the eigenstructure of the five-equation system.
First, the eigenvalues employed by (Ferrari *et al.*, 2017) are

$$\boldsymbol{\lambda} = \begin{bmatrix} u_\mathrm{i} \\ u_g - c_g \\ u_g + c_g \\ u_l - c_l \\ u_l + c_l \end{bmatrix}, \tag{18}$$

while the ones adopted in the present work are

$$\boldsymbol{\lambda} = \begin{bmatrix} u_\mathrm{i} \\ \frac{u_g}{2}(1+\gamma_g) - \frac{\sqrt{4c_g^2+[u_g(\gamma_g-1)]^2}}{2} \\ \frac{u_g}{2}(1+\gamma_g) + \frac{\sqrt{4c_g^2+[u_g(\gamma_g-1)]^2}}{2} \\ \frac{u_l}{2}(1+\gamma_l) - \frac{\sqrt{4c_l^2+[u_l(\gamma_l-1)]^2}}{2} \\ \frac{u_l}{2}(1+\gamma_l) + \frac{\sqrt{4c_l^2+[u_l(\gamma_l-1)]^2}}{2} \end{bmatrix}, \tag{19}$$

where $c_g = 316.22\ m/s$ and $c_l = 1000\ m/s$ are the speed of sound respectively for gas and liquid phase.
The eigenvectors without the shape factors are

$$\mathbf{R} = \begin{bmatrix} 1 & 0 & 0 & 0 & 0 \\ -\frac{c_g^2\rho_g+\alpha_g\rho_g\zeta}{[(u_g-u_\mathrm{i})^2-c_g^2]} & 1 & 1 & 0 & 0 \\ -\frac{c_g^2\rho_g+\alpha_g\rho_g\zeta}{[(u_g-u_\mathrm{i})^2-c_g^2]}u_\mathrm{i} & u_g-c_g & u_g+c_g & 0 & 0 \\ \frac{c_l^2\rho_l-\alpha_l\rho_l\zeta}{[(u_l-u_\mathrm{i})^2-c_l^2]} & 0 & 0 & 1 & 1 \\ \frac{c_l^2\rho_l-\alpha_l\rho_l\zeta}{[(u_l-u_\mathrm{i})^2-c_l^2]}u_\mathrm{i} & 0 & 0 & u_l-c_l & u_l+c_l \end{bmatrix}, \tag{20}$$

where $\zeta = -\frac{\pi D g \cos\theta}{4\sin(\beta)}$; the eigenvectors including γ factors are

$$\mathbf{R} = \begin{bmatrix} 1 & 0 & 0 & 0 & 0 \\ r_{21} & 1 & 1 & 0 & 0 \\ r_{31} & \frac{\gamma_g u_g^2-c_g^2}{\lambda_3} & \frac{\gamma_g u_g^2-c_g^2}{\lambda_2} & 0 & 0 \\ r_{41} & 0 & 0 & 1 & 1 \\ r_{51} & 0 & 0 & \frac{\gamma_l u_l^2-c_l^2}{\lambda_5} & \frac{\gamma_l u_l^2-c_l^2}{\lambda_4} \end{bmatrix}, \tag{21}$$

with

$$\begin{aligned} r_{21} &= -\frac{c_g^2\rho_g+\alpha_g\rho_g\zeta}{[\gamma_g u_g^2 - u_g u_\mathrm{i}(1+\gamma_g)+u_\mathrm{i}^2-c_g^2]}, \\ r_{31} &= -\frac{c_g^2\rho_g+\alpha_g\rho_g\zeta}{[\gamma_g u_g^2 - u_g u_\mathrm{i}(1+\gamma_g)+u_\mathrm{i}^2-c_g^2]}u_\mathrm{i}, \\ r_{41} &= \frac{c_l^2\rho_l-\alpha_l\rho_l\zeta}{[\gamma_l u_l^2 - u_l u_\mathrm{i}(1+\gamma_l)+u_\mathrm{i}^2-c_l^2]}, \\ r_{51} &= \frac{c_l^2\rho_l-\alpha_l\rho_l\zeta}{[\gamma_l u_l^2 - u_l u_\mathrm{i}(1+\gamma_l)+u_\mathrm{i}^2-c_l^2]}u_\mathrm{i}. \end{aligned} \tag{22}$$

It is possible to observe that, when in Equations (19) and (21) γ_g and γ_l are unitary, the expressions without the shape factor of Equations (18) and (20) are recovered. Therefore, the eigenstructure of the model including shape factors can be seen as an extension of the one by (Ferrari *et al.*, 2017).

APPENDIX B: FURTHER EQUATIONS ADOPTED IN THE MODEL

In this Appendix, we report the equations developed by (Biberg, 2007) and adopted in the presented model.
Δ_j and C_j, adopted in Eq. (7), are (the subscript j has been removed for clarity)

$$\begin{aligned}\Delta &= \ln(1-Y) + \frac{(K^3+R^3)\ln(Y+K(1-Y))}{|R|^{5/2}-K^3} \\ &+ \frac{(R+\sqrt{|R|})\sqrt[3]{|R|}ln(Y+|R|^{5/6}(1-Y))}{3(K-|R|^{5/6})} \\ &- (R+\sqrt{|R|})(K+2|R|^{5/6})|R|^{5/6}\sqrt[3]{|R|} \\ &\cdot \frac{\ln Y^2-(1-Y)(Y-(1-Y)|R|^{5/6})}{6(K^2+|R|^{5/6}K+|R|^{5/3})} \\ &+ \frac{K(R+\sqrt{|R|})\sqrt[3]{|R|}}{\sqrt{3}(K^2+|R|^{5/6}K+|R|^{5/3})} \\ &\cdot \tan^{-1}\left(\frac{2(Y-1)|R|^{5/3}+(2Y-1)|R|^{5/6}+2Y}{\sqrt{3}|R|^{5/6}}\right) \end{aligned} \quad (23)$$

and

$$C = C^1 + sgn(\tau_w)\frac{u^*}{\kappa}\psi, \quad (24)$$

where

$$C^1 = sgn(\tau_w)\frac{u^*}{\kappa}\left(\ln\left(\frac{h}{k_s}\right)+A\kappa\right), \quad (25)$$

and

$$\psi = -\frac{K(R+\sqrt{|R|})\sqrt[3]{|R|}}{\sqrt{3}(K^2+|R|^{5/6}K+|R|^{5/3})}\tan^{-1}\left(\frac{1+2/|R|^{5/6}}{\sqrt{3}}\right). \quad (26)$$

The exponent $F(R_j,K_j)$ reported in Eq. (11) is (the subscript j has been removed for clarity)

$$F(R,K) = \frac{\Lambda+\psi}{\Lambda^P}, \quad (27)$$

where

$$\begin{aligned}\Lambda &= \frac{5(R+\sqrt{|R|})(|R|^{5/2}+K^2+K)R^2\ln(|R|)}{6(K^3-|R|^{5/2})(|R|^{5/2}-1)} \\ &- \frac{K(K^3+R^3)\ln(K)}{(K-1)(K^3-|R|^{5/2})} \\ &+ \frac{(R+\sqrt{|R|})\sqrt[3]{|R|}}{\sqrt{3}(|R|^{5/3}+|R|^{5/6}+1)(K^2+K|R|^{5/6}+|R|^{5/3})} \\ &\cdot \left((K-|R|^{5/3})\tan^{-1}\left(\frac{1+2/|R|^{5/6}}{\sqrt{3}}\right)\right. \\ &\left.- (K+(K+1)|R|^{5/6})|R|^{5/6}\tan^{-1}\left(\frac{2|R|^{5/6}+1}{\sqrt{3}}\right)\right), \end{aligned} \quad (28)$$

and

$$\Lambda^P = -\frac{2}{27}(2\sqrt{3}+9). \quad (29)$$